

YUNIC: A Multi-Dimensional Particle-In-Cell Code for Laser-Plasma Interaction

Huai-Hang Song,¹ Wei-Min Wang,² and Yu-Tong Li¹

¹*Beijing National Laboratory for Condensed Matter Physics,
Institute of Physics, Chinese Academy of Sciences, Beijing 100190, China*

²*Department of Physics and Beijing Key Laboratory of
Opto-electronic Functional Materials and Micro-nano Devices,
Renmin University of China, Beijing 100872, China*

(Dated: April 2, 2021)

Abstract

For simulating laser-plasma interactions, we developed a parallel, multi-dimensional, fully relativistically particle-in-cell (PIC) code, named YUNIC. The core algorithm is introduced, including field solver, particle pusher, field interpolation, and current interpolation. In addition to the classical electromagnetic interaction in plasmas, nonlinear Compton scattering and nonlinear Breit-Wheeler pair production are also implemented based on Monte-Carlo methods to study quantum electrodynamics (QED) processes. We benchmark YUNIC against theories and other PIC codes through several typical cases. YUNIC can be applied in varieties of physical scenes, from relativistic laser-plasma interactions to astrophysical plasmas and strong-field QED physics.

CONTENTS

I. Introduction	2
II. Standard particle-in-cell algorithm	3
A. Normalization	3
B. Field solver	4
C. Particle pusher	5
D. Field interpolation	6
E. Current interpolation	7
F. Algorithm structure	7
III. Benchmarks in several typical cases	8
IV. QED modules	10
V. Conclusion	13
Acknowledgments	14
References	14

I. INTRODUCTION

The particle-in-cell (PIC) method [1], belonging to a kinetic description, can accurately simulate the collective plasma behavior, from linear to relativistically nonlinear processes. Compared to magnetohydrodynamics simulation, PIC simulation utilizing the quasi-particle concept can resolve plasma dynamics on smaller spatial and temporal scales. Meanwhile, it requires much less computational expense than that by directly solving Vlasov-Boltzmann equations. Since it was initially developed in 1970s [2], PIC method has become one of the most powerful and indispensable tools in various plasma areas, particularly in laser-plasma interactions [3, 4]. In this manuscript, we introduce a recently developed PIC code YUNIC, and demonstrate a few typical benchmarks to validate this code. Besides the classical plasma dynamics, YUNIC is also capable of simulating extremely laser-plasma interactions in the quantum electrodynamics (QED) regime, including spin and polarization effects in

the processes of nonlinear Compton scattering and nonlinear Breit-Wheeler pair production [5].

II. STANDARD PARTICLE-IN-CELL ALGORITHM

The core idea of PIC method is to solve Maxwell's equations on the discrete spatial grid [Sec. II B], while pushing quasi-particles in the free space [Sec. II C]. The currents generated by moving charged particles should be interpolated to the spatial grid as sources to solve field equations [Sec. II E], and fields should also be interpolated back to an arbitrary particle position to push them [Sec. II D]. Hence, the discrete fields and non-discrete particles are self-consistently connected. The main equations for solving collisionless plasma problems are as follows (in Gaussian units):

$$\nabla \cdot \mathbf{E} = 4\pi\rho, \quad (1)$$

$$\nabla \cdot \mathbf{B} = 0, \quad (2)$$

$$\nabla \times \mathbf{E} = -\frac{1}{c} \frac{\partial \mathbf{B}}{\partial t}, \quad (3)$$

$$\nabla \times \mathbf{B} = \frac{1}{c} \left(4\pi\mathbf{J} + \frac{\partial \mathbf{E}}{\partial t} \right), \quad (4)$$

$$\frac{\partial \rho}{\partial t} + \nabla \cdot \mathbf{J} = 0, \quad (5)$$

$$\frac{d\mathbf{p}}{dt} = q(\mathbf{E}_p + \frac{\mathbf{p}}{\gamma mc} \times \mathbf{B}_p), \quad (6)$$

$$\frac{d\mathbf{x}_p}{dt} = \frac{\mathbf{p}}{\gamma m}, \quad (7)$$

where Eqs. (1)-(4) are Maxwell's equations, Eq. (5) is the charge conservation equation, Eqs. (6) and (7) are Newton-Lorentz equations.

A. Normalization

In the PIC code, after defining a reference frequency ω_r , it is convenient to normalize time t , length L , electric field \mathbf{E} , magnetic field \mathbf{B} , particle velocity \mathbf{v} , momentum \mathbf{p} , number density n , current density \mathbf{J} , charge q and mass m to following quantities, respectively:

$$\begin{aligned} t_r &= \frac{1}{\omega_r}, & L_r &= \frac{c}{\omega_r}, & E_r &= \frac{m_e c \omega_r}{e}, & B_r &= \frac{m_e c \omega_r}{e}, & v_r &= c, \\ p_r &= m_e c, & n_r &= \frac{m_e \omega_r^2}{4\pi e^2}, & J_r &= c e n_r, & q_r &= e, & m_r &= m_e, \end{aligned} \quad (8)$$

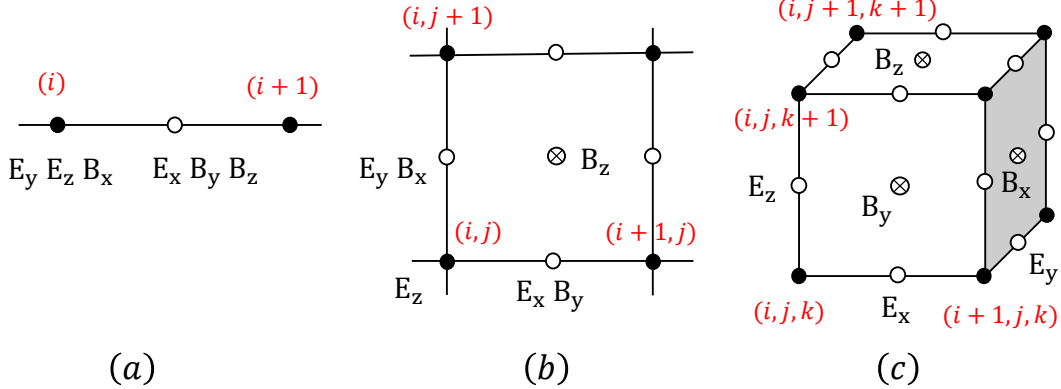


FIG. 1. The staggered Yee grid in (a) one dimensional (1D), (b) two dimensional (2D), and (c) three dimensional (3D) spaces for solving Maxwell's equations, respectively.

where m_e is the electron rest mass, and e is the electron charge. In laser-plasma interactions, ω_r is usually chosen as the laser frequency ω_L , and it could also be chosen as the plasma oscillating frequency ω_p in other interactions. For convenience, we use normalized quantities below based on Eq. (8).

B. Field solver

The electromagnetic fields \mathbf{E} and \mathbf{B} are self-consistently evolved by solving Maxwell's equations. One only needs to solve two curl equations [Eqs. (3) and (4)] and a charge conservation equation [Eq. (5)], because the other two divergence equations [Eqs. (1) and (2)] are automatically satisfied with time if they hold initially [6, 7]. The details of how to realize the charge conservation are presented in Sec. II E.

The finite-difference time-domain (FDTD) method [8] is adopted for numerically solving Maxwell's equations. Equations. (3) and (4) can be written as the following discrete forms with the 2nd-order accuracy:

$$\mathbf{E}^{n+1/2} - \mathbf{E}^{n-1/2} = \Delta t(\nabla \times \mathbf{B}^n - \mathbf{J}^n), \quad (9)$$

$$\mathbf{B}^{n+1} - \mathbf{B}^n = -\Delta t \nabla \times \mathbf{E}^{n+1/2}. \quad (10)$$

Here, the leapfrog scheme is adopted in time and the famous staggered Yee grid [9] is employed in space, as illustrated in Fig. 1.

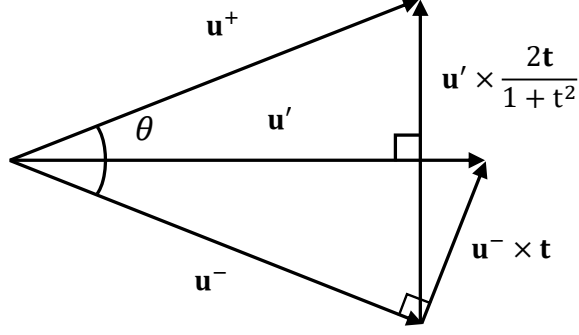


FIG. 2. Diagram of Boris algorithm.

C. Particle pusher

We proceed to solve the motion of charged particles in the electromagnetic field by discretizing Eqs. (6) and (7) as following:

$$\frac{\mathbf{u}^{n+1} - \mathbf{u}^n}{\Delta t} = q_m (\mathbf{E}_p^{n+1/2} + \frac{1}{\gamma^{n+1/2}} \mathbf{u}^{n+1/2} \times \mathbf{B}_p^{n+1/2}), \quad (11)$$

$$\frac{\mathbf{r}_p^{n+3/2} - \mathbf{r}_p^{n+1/2}}{\Delta t} = \frac{\mathbf{u}^{n+1}}{\gamma^{n+1}}, \quad (12)$$

where $\mathbf{u} = \mathbf{p}/m$ and $q_m = q/m$.

Boris algorithm [10] is employed to push charged particles due to its advantage of long term accuracy [11], which splits the electric and magnetic forces by defining \mathbf{u}^+ and \mathbf{u}^- ,

$$\mathbf{u}^n = \mathbf{u}^- - \frac{q_m \Delta t}{2} \mathbf{E}_p^{n+1/2}, \quad (13)$$

$$\mathbf{u}^{n+1} = \mathbf{u}^+ + \frac{q_m \Delta t}{2} \mathbf{E}_p^{n+1/2}. \quad (14)$$

Substituting Eqs. (13) and (14) into Eq. (11), one can obtain a rotation equation of \mathbf{u}^+ and \mathbf{u}^- about the magnetic field \mathbf{B}_p , i.e., $2\gamma^{n+1/2}(\mathbf{u}^+ - \mathbf{u}^-) = q_m \Delta t (\mathbf{u}^+ + \mathbf{u}^-) \times \mathbf{B}_p^{n+1/2}$, and then solve it by the following implementation:

$$\mathbf{u}' = \mathbf{u}^- + \mathbf{u}^- \times \mathbf{t}, \quad (15)$$

$$\mathbf{u}^+ = \mathbf{u}^- + \mathbf{u}' \times \frac{2\mathbf{t}}{1+t^2} \quad (16)$$

where $\mathbf{t} = q_m \Delta t \mathbf{B}_p^{n+1/2} / (2\gamma^{n+1/2})$. The diagram of Boris algorithm is illustrated in Fig. 2.

If contributions of electric field and magnetic field to the Lorentz force nearly cancel out, e.g., in the rest frame of an ultrarelativistic beam [12], Boris algorithm might lead to large errors, and Vay algorithm [13] is more suitable.

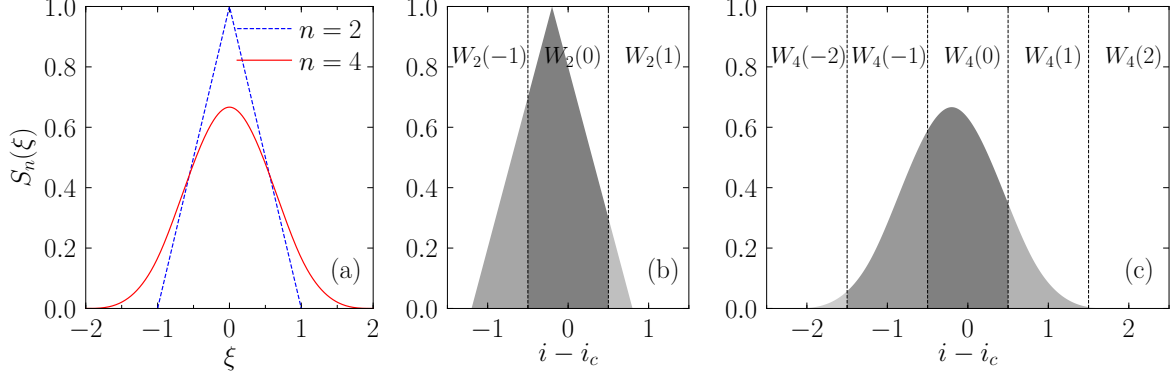


FIG. 3. (a) Shape functions $S_n(\xi)$ of 2nd-order ($n = 2$) and 4th-order ($n = 4$) used in PIC for field and current interpolations. (b) (c) The area of the shadow $W_n(i - i_c)$ represents the weight of the grid field acting on the particle for $n = 2$ and $n = 4$, respectively. Normally, weight function $W_2(i - i_c)$ crosses three grid cells, and $W_4(i - i_c)$ crosses five grid cells.

D. Field interpolation

In Sec. II C, we have discussed how to push a charged particle provided we have known the electric field \mathbf{E}_p and magnetic field \mathbf{B}_p at the particle position $\mathbf{r}_p(x_p, y_p, z_p)$. In this section, we discuss how to obtain \mathbf{E}_p and \mathbf{B}_p through the interpolation. Actually, it depends on the interpolation shape function $S_n(\xi)$ we choose, where n is the interpolation order. The function $S_n(\xi)$ defines the shape and smoothness of quasi-particles and also determines the simulation accuracy [1]. Taking 1D as an example, its 2nd-order and 4th-order forms shown in Fig. 3(a) are given by [14]

$$S_2(\xi) = \begin{cases} 1 - |\xi| & \text{if } |\xi| \leq 1, \\ 0 & \text{otherwise,} \end{cases} \quad (17)$$

$$S_4(\xi) = \begin{cases} \frac{2}{3} - |\xi|^2 + \frac{1}{2}|\xi|^3 & \text{if } |\xi| \leq 1, \\ \frac{4}{3}(1 - \frac{1}{2}|\xi|)^3 & \text{if } 1 < |\xi| \leq 2, \\ 0 & \text{otherwise.} \end{cases} \quad (18)$$

For a particle located at x_p , its acting field contributed by grid point i can be expressed as $F(i) * W_n(i - i_c)$, where its weight function is defined by $W_n(i - i_c) = \int_{i-1/2}^{i+1/2} S_n(\xi - x_p/\Delta x) d\xi$ and i_c is the grid point nearest to the particle, as shown in Figs. 3(b) and 3(c). The expression of $W_n(i - i_c)$ after the integration can be found from APPENDIX A of [14].

In 3D, the electromagnetic field acting on the particle can be calculated through following interpolations under the condition that the fields are constant over each cell:

$$\mathbf{E}(\mathbf{B})_p(x_p, y_p, z_p) = \sum_{i,j,k} W_n(i - i_c) * W_n(j - j_c) * W_n(k - k_c) * \mathbf{E}(\mathbf{B})(i, j, k). \quad (19)$$

Notice that different field components generally have different weights since the grid is staggered [see Fig. 1].

E. Current interpolation

As we mentioned in Sec. II B, one needs to ensure the charge conservation in order to avoid solving Poisson's equation [Eq. (1)] [7], since the local computation of the former is much simpler and computationally cheaper than the global computation of the latter. In YUNIC, Esirkepov algorithm [15] is adopted to ensure the charge conservation in the current calculation. By assuming the particle trajectory over one time step is a straight line, the current flux in 3D is decomposed into twelve segments along x , y , and z axes, respectively, i.e.,

$$J_x^{n+1}(i + 1, j, k) - J_x^{n+1}(i, j, k) = -q \frac{\Delta x}{\Delta t} W_x(i, j, k), \quad (20)$$

$$J_y^{n+1}(i, j + 1, k) - J_y^{n+1}(i, j, k) = -q \frac{\Delta y}{\Delta t} W_y(i, j, k), \quad (21)$$

$$J_z^{n+1}(i, j, k + 1) - J_z^{n+1}(i, j, k) = -q \frac{\Delta z}{\Delta t} W_z(i, j, k), \quad (22)$$

where $W_x(i, j, k)$, $W_y(i, j, k)$ and $W_z(i, j, k)$ can be found from Eq. (31) in [15].

This method is easily extended to an arbitrary high-order shape function $S_n(\xi)$. Note that $S_n(\xi)$ employed in the current interpolation should be the same as that in the field interpolation [Sec. II D] to eliminate the self-force.

F. Algorithm structure

YUNIC is written in C++ language and massively parallelized by MPI. The simulation results are output in parallel by MPI-IO and then analyzed/visualized by Python/Matplotlib. Its three versions aimed at different spatial dimensions (1D, 2D, and 3D) are constructed separately for efficiency. YUNIC employs a modified algorithm that originally adopted in PSC [16] by Hartmut Ruhl, and latter also adopted in EPOCH [17], which is slightly different

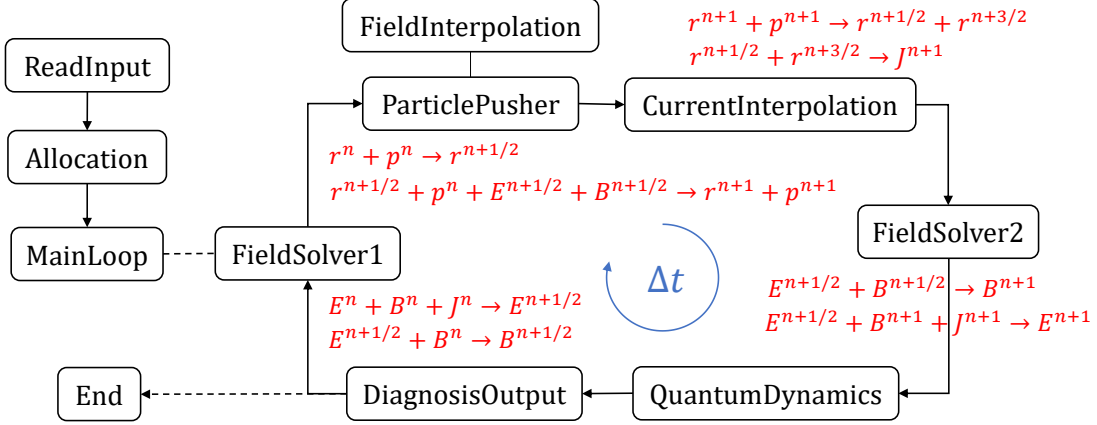


FIG. 4. Flow chart of the core algorithm in YUNIC.

from the common algorithm as described in Secs. II B–II E. The modified algorithm updates the fields and particle positions at both full-time steps and half-time steps, as sketched in Fig. 4. Hence, the drawback of the leapfrog method is overcome and one can obtain the information of fields and particles at the same time, which is important in some cases, e.g., for simulating QED processes.

III. BENCHMARKS IN SEVERAL TYPICAL CASES

Here, we benchmark our PIC code YUNIC against the open-source PIC code SMILEI [18], including 1D, 2D and 3D versions. At these presented cases, the simulation results of two PIC codes are in good agreement.

(a) *1D PIC simulation: hole boring.* A linearly (circularly) polarized laser with a wavelength of $\lambda_L = 1 \mu\text{m}$ incidents from the left boundary at $t = 0$ ps. The laser has a 5-laser-period rise time before a constant normalized intensity of $a_0 = eE_L/m_e c\omega_L = 10\sqrt{2}$ (10). An uniform overdense plasma with an electron density of $n_p = 50n_c$ is located at $5 \mu\text{m} < x < 15 \mu\text{m}$, where $n_c = m_e\omega_L^2/4\pi e^2$. The computational domain has a size of $20\lambda_L$ with 5120 cells in the x direction. Each cell contains 100 electrons and 100 protons. Absorbing boundaries are used for both particles and fields. The 4th-order interpolation is employed. The comparison of ion charge density n_i at different times are shown in Fig. 5.

(b) *2D PIC simulation: self-heating.* A plasma with an initial temperature of 1 keV has an uniform electron density of $n_p = 100n_c$. Each plasma wavelength ($\lambda_p = 2\pi/k_p$) contains 320 grids. Periodic boundaries are applied for both particles and fields. No current

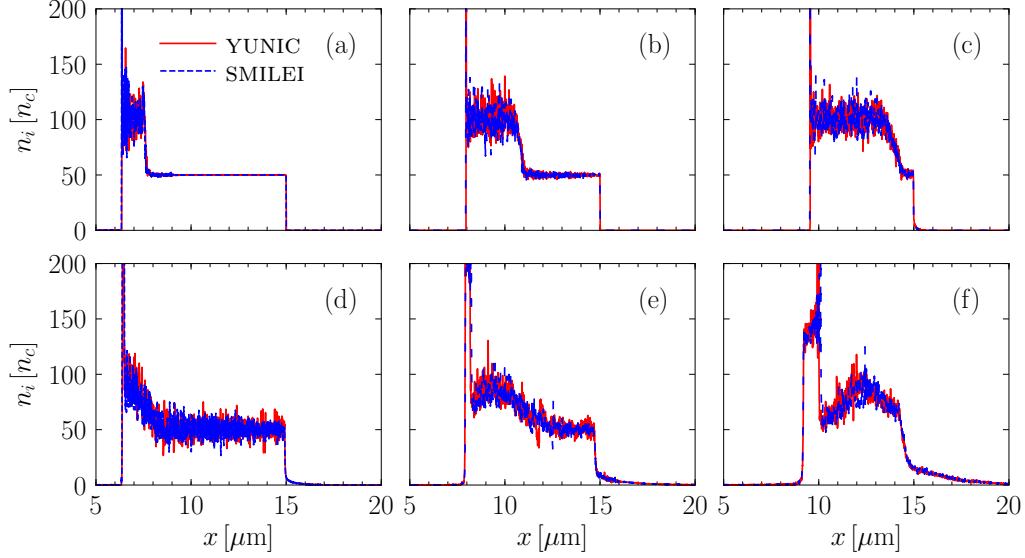


FIG. 5. Spatial distributions of ion density n_i at different times, (a)(d) $t = 0.17$ ps, (b)(e) $t = 0.33$ ps, and (c)(f) $t = 0.5$ ps. (a)-(c) and (d)-(f) correspond to circularly and linearly polarized lasers, respectively.

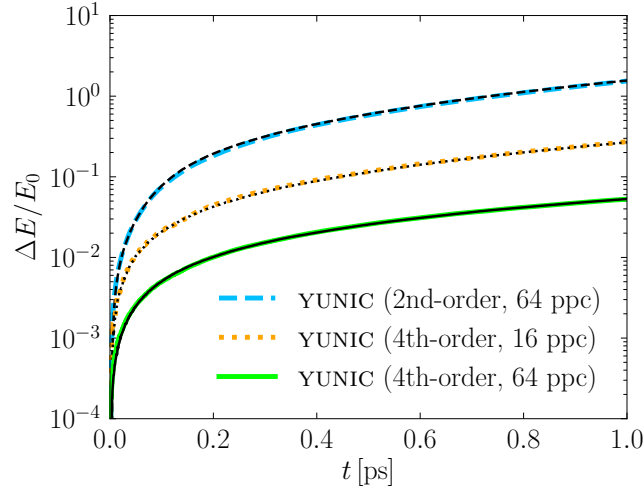


FIG. 6. Time evolution of the relative increase of total energy $\Delta E/E_0$ with different interpolation orders and particles per cell (ppc). The colored thick lines are the simulation results by YUNIC, and black thin lines correspond to those by SMILEI.

smoothing or other additional algorithms are used to control self-heating. The comparison of relative energy increasing $\Delta E/E_0$ due to self-heating are shown in Fig. 6.

(c) *3D PIC simulation: wakefield driven by electron or positron beam.* A 1-GeV drive electron (positron) beam has a bi-Gaussian density profile with a transverse size $k_p \sigma_r = 0.5$,

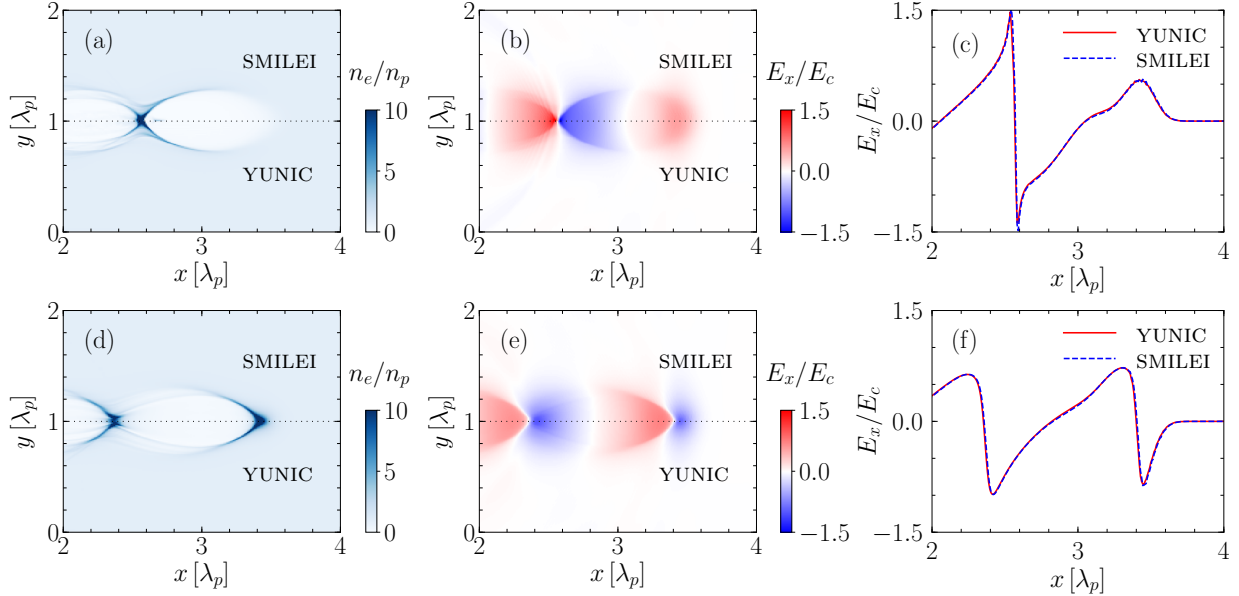


FIG. 7. (a)(d) Electron density n_e of the background plasma. (b)(e) Longitudinal electric field E_x . (c)(f) On-axis distribution of E_x . (a)-(c) and (d)-(f) are driven by electron and positron beams, respectively.

bunch length $k_p\sigma_x = 0.5$, and peak density $n_b/n_p = 4$. The computational domain has a size of $4\lambda_p \times 2\lambda_p \times 2\lambda_p$ in $x \times y \times z$ directions, sampled by $512 \times 192 \times 192$ cells. Each cell contains 8 electrons and 8 protons for the uniform background plasma and 4 electrons or positrons for the drive beam. For the field initialization of an ultrarelativistic charged beam, YUNIC first solves the Poisson's equation in the beam's rest frame, and then applies Lorentz transformation to obtain its self-generated fields in the laboratory frame [19]. The comparison of background plasma density n_e and excited longitudinal electric field E_x are shown in Fig. 7.

IV. QED MODULES

The available petawatt and next-generation 10-petawatt and 100-petawatt laser systems can provide an extreme field density of $I_0 = 10^{22-25} \text{W/cm}^2$. To explore interactions of ultraintense lasers with plasmas, YUNIC have implemented QED modules with Monte-Carlo methods [20–22] to calculate the photon emission via nonlinear Compton scattering and the electron-positron pair production via nonlinear Breit-Wheeler process.

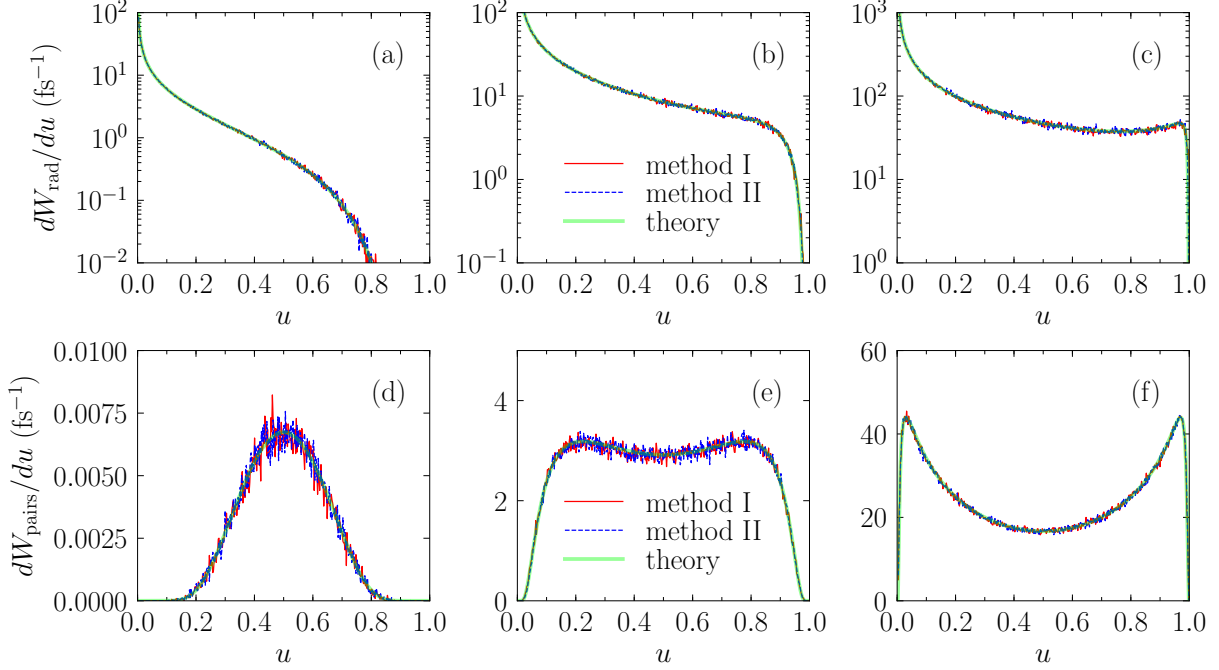


FIG. 8. (Upper row) The spectra of emitted photons with $\varepsilon_e = 510$ MeV and (a) $\chi_e = 0.49$, (b) $\chi_e = 4.9$, and (c) $\chi_e = 49$, respectively. (Lower row) The spectra of generated positrons with $\varepsilon_\gamma = 510$ MeV and (d) $\chi_\gamma = 0.49$, (e) $\chi_\gamma = 4.9$, and (f) $\chi_\gamma = 49$, respectively.

The spin- and polarized-averaged differential probability of the photon emission is written as [5]

$$\frac{d^2 W_{\text{rad}}}{dudt} = \frac{\alpha m^2 c^4}{\sqrt{3} \pi \hbar \varepsilon_e} \left[\frac{u^2 - 2u + 2}{1 - u} K_{2/3}(y) - \int_y^\infty K_{1/3}(x) dx \right], \quad (23)$$

where $K_\nu(y)$ is the second-kind ν -order modified Bessel function, $y = 2u/[3(1-u)\chi_e]$, $u = \varepsilon_\gamma/\varepsilon_e$, ε_e is the electron energy before the photon emission, ε_γ is the emitted photon energy, and $\alpha \approx 1/137$ is the fine structure constant. Quantum parameter $\chi_e = (e\hbar/m_e^3 c^4)|F_{\mu\nu}p^\nu|$ presents the field experienced by the electron in its rest frame normalized to the Schwinger critical field $E_{\text{cr}} = 1.3 \times 10^{16}$ V/cm or $B_{\text{cr}} = 4.4 \times 10^{13}$ G. The laser-plasma interaction enters the QED-dominated region if $\chi_e \gtrsim 1$.

To calculate Eq. (23), two different Monte-Carlo methods have been implemented in YUNIC. Both methods require two uniformly distributed random numbers r_1 and r_2 to simulate the stochastic photon emission, where $r_1, r_2 \in (0, 1)$. Method I [20]: First, a random number r_1 is generated to compare with the total radiation probability W_{rad} ; if $r_1 > W_{\text{rad}}$, a photon is emitted, and its energy ratio u_0 is determined by the other random

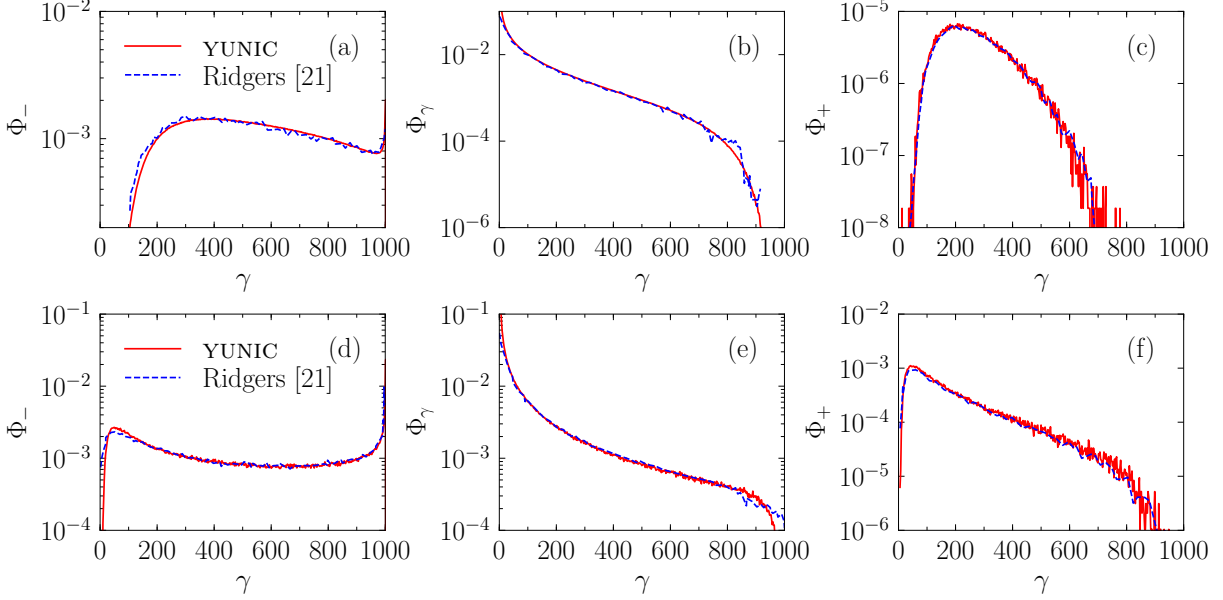


FIG. 9. Energy spectra of (a)(d) electrons Φ_- , (b)(e) photons Φ_γ , and (c)(f) positrons Φ_+ . (a)-(c) and (d)-(f) correspond to strengths of the external magnetic field $B_0 = 0.001B_{\text{cr}}$ and $B_0 = 0.009B_{\text{cr}}$, respectively.

number r_2 according to $\int_{u_{\text{min}}}^{u_0} dW_{\text{rad}}/du = r_2 W_{\text{rad}}$ with a low-energy cutoff u_{min} . Method II [20, 22]: a photon with an energy ratio of $u_0 = r_1^3$ is emitted if $3r_1^2 dW_{\text{rad}}(u_0)/du > r_2$. The photon spectrum calculated by two methods are both in good agreement with the theoretical spectrum of Eq. (23), as shown in Figs. 8(a)-(c).

Similarly, the spin- and polarized-averaged differential probability of the pair production is written as [5]

$$\frac{d^2 W_{\text{pairs}}}{d\varepsilon_+ dt} = \frac{\alpha m^2 c^4}{\sqrt{3}\pi \hbar \varepsilon_\gamma^2} \left[\frac{\varepsilon_+^2 + \varepsilon_-^2}{\varepsilon_+ \varepsilon_-} K_{2/3}(y) + \int_y^\infty K_{1/3}(x) dx \right], \quad (24)$$

where $y = 2\varepsilon_\gamma^2/(3\chi_\gamma \varepsilon_+ \varepsilon_-)$, and ε_γ , ε_- and ε_+ are the energies of the parent γ photon, newly created electron and positron, respectively. Another parameter $\chi_\gamma = (e\hbar^2/m_e^3 c^4)|F_{\mu\nu}k^\nu|$ characterizes the pair production. Two Monte-Carlo methods for the photon emission discussed above are also employed to calculate the pair production in the similar way, which are in good agreement with the theory, as shown in Figs. 8(d)-(f).

Now, we benchmark our QED module in the process of electron-positron cascades with just Method II, where the photon emission, quantum radiation reaction, and pair production are self-consistently included. In Fig. 9, we consider the same simulation setups as Fig. 2 and Fig. 4 of [21], where an electron bunch of an initial Lorentz factor $\gamma_0 = 1000$ are

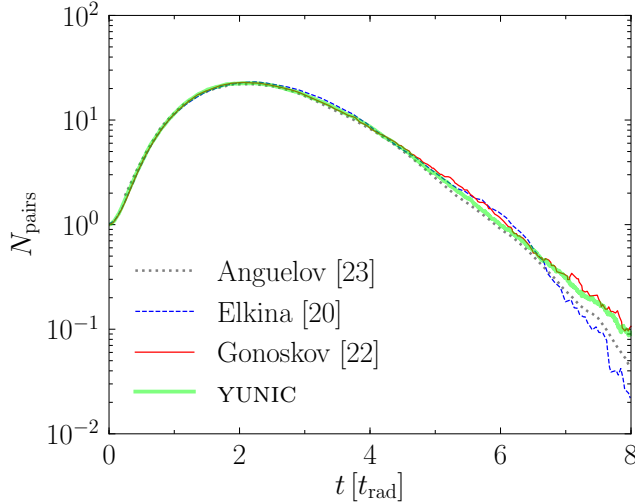


FIG. 10. The number of pairs of energies above 200 MeV, where $t_{\text{rad}} = 1.16 \times 10^{-16}$ s.

moving under a perpendicularly external magnetic field of a strength of $B_0 = 0.001B_{\text{cr}}$ or $B_0 = 0.009B_{\text{cr}}$. The energy spectra of electrons, photons and positrons both agree well with the results of [21].

In Fig. 10, we present a typical cascade case to further test our QED module. An electron with an initial Lorentz factor $\gamma_0 = 2 \times 10^5$ is moving under a perpendicularly external magnetic field of a strength of $B_0 = 0.2B_{\text{cr}}$. The total number of electrons and positrons of energies above 100 MeV are countered. The simulation result is shown in Fig. 10, which is averaged over 2000 simulation runs with different random seeds. Our simulation result is in good agreement with those in [20, 22, 23].

The electron/positron spin and γ -photon polarization are also implemented into the QED module of YUNIC [24–26] based on spin- and polarization resolved photon emission and pair production probabilities [5, 27–29], which have been benchmarked in [25]. Hence, YUNIC can be used to investigate spin and polarization related effects in laser-plasma interactions, which are ignored in the previously employed QED-PIC.

V. CONCLUSION

In summary, we have introduced a multi-dimensional PIC code, named YUNIC. Its core algorithm is described and several benchmarks are preformed. YUNIC was employed to investigate the low-frequency whistler waves excited by relativistic laser pulses [30] and

the spin and polarization effects on the nonlinear Breit-Wheeler pair production in laser-plasma interactions [26]. In the future, YUNIC will continue to be used to explore interesting phenomena or physical processes of application prospects and new physical modules may be added for specific problems.

ACKNOWLEDGMENTS

This work was supported by the National Key R&D Program of China (Grant No. 2018YFA0404801), National Natural Science Foundation of China (Grant Nos. 11775302 and 11721091), the Strategic Priority Research Program of Chinese Academy of Sciences (Grant Nos. XDA25050300, XDA25010300).

-
- [1] Charles K Birdsall and A Bruce Langdon, *Plasma Physics via Computer Simulation* (Institute of Physics, Bristol, 1991).
 - [2] John M. Dawson, “Particle simulation of plasmas,” *Rev. Mod. Phys.* **55**, 403–447 (1983).
 - [3] Paul Gibbon, *Short Pulse Laser Interactions with Matter* (Imperial College Press, London, 2005).
 - [4] A. Macchi, *A Superintense Laser-Plasma Interaction Theory Primer* (Springer, 2013).
 - [5] V. N. Baier, V.M. Katkov, and V. M. Strakhovenko, *Electromagnetic Processes at High Energies in Oriented Single Crystals* (World Scientific, Singapore, 1998).
 - [6] James W. Eastwood, “The virtual particle electromagnetic particle-mesh method,” *Comput. Phys. Commun.* **64**, 252–266 (1991).
 - [7] John Villasenor and Oscar Buneman, “Rigorous charge conservation for local electromagnetic field solvers,” *Comput. Phys. Commun.* **69**, 306–316 (1992).
 - [8] A. Taflove and S. C. Hagness, *Computational Electromagnetics: The Finite-Difference Time-Domain Method* (Artech House, Boston, 2000).
 - [9] Kane Yee, “Numerical solution of initial boundary value problems involving maxwell’s equations in isotropic media,” *IEEE Trans. Antennas Propag.* **14**, 302–307 (1966).
 - [10] J. P. Boris, “Proceedings of 4th conference on numerical simulation of plasmas,” (Naval Research Laboratory, Washington D. C., 1970) p. 3–67.

- [11] Hong Qin, Shuangxi Zhang, Jianyuan Xiao, Jian Liu, Yajuan Sun, and William M. Tang, “Why is Boris algorithm so good?” *Phys. Plasmas* **20**, 084503 (2013).
- [12] J.-L. Vay, “Noninvariance of space- and time-scale ranges under a Lorentz transformation and the implications for the study of relativistic interactions,” *Phys. Rev. Lett.* **98**, 130405 (2007).
- [13] J.-L. Vay, “Simulation of beams or plasmas crossing at relativistic velocity,” *Phys. Plasmas* **15**, 056701 (2008).
- [14] Hirotsada Abe, Natsuhiko Sakairi, Ryohei Itatani, and Hideo Okuda, “High-order spline interpolations in the particle simulation,” *J. Comput. Phys.* **63**, 247–267 (1986).
- [15] T. Zh. Esirkepov, “Exact charge conservation scheme for Particle-in-Cell simulation with an arbitrary form-factor,” *Comput. Phys. Commun.* **135**, 144 – 153 (2001).
- [16] Hartmut Ruhl, *Classical Particle Simulations with the PSC code*.
- [17] T. D. Arber, K. Bennett, C. S. Brady, A. Lawrence-Douglas, M. G. Ramsay, N. J. Sircombe, P. Gillies, R. G. Evans, H. Schmitz, A. R. Bell, and C. P. Ridgers, “Contemporary particle-in-cell approach to laser-plasma modelling,” *Plasma Phys. Control. Fusion* **57**, 113001 (2015).
- [18] J. Derouillat, A. Beck, F. Pérez, T. Vinci, M. Chiaramello, A. Grassi, M. Flé, G. Bouchard, I. Plotnikov, N. Aunai, J. Dargent, C. Riconda, and M. Grech, “Smilei : A collaborative, open-source, multi-purpose particle-in-cell code for plasma simulation,” *Comput. Phys. Commun.* **222**, 351–373 (2018).
- [19] F. Massimo, A. Marocchino, and A.R. Rossi, “Electromagnetic self-consistent field initialization and fluid advance techniques for hybrid-kinetic PWFA code Architect,” *Nucl. Instrum. Methods A* **829**, 378–382 (2016), 2nd European Advanced Accelerator Concepts Workshop - EAAC 2015.
- [20] N. V. Elkina, A. M. Fedotov, I. Yu. Kostyukov, M. V. Legkov, N. B. Narozhny, E. N. Nerush, and H. Ruhl, “QED cascades induced by circularly polarized laser fields,” *Phys. Rev. ST Accel. Beams* **14**, 054401 (2011).
- [21] C. P. Ridgers, J. G. Kirk, R. Duclous, T. G. Blackburn, C. S. Brady, K. Bennett, T. D. Arber, and A. R. Bell, “Modelling gamma-ray photon emission and pair production in high-intensity laser–matter interactions,” *J. Comput. Phys.* **260**, 273–285 (2014).
- [22] A. Gonoskov, S. Bastrakov, E. Efimenko, A. Ilderton, M. Marklund, I. Meyerov, A. Muraviev, A. Sergeev, I. Surmin, and E. Wallin, “Extended particle-in-cell schemes for physics in ultrastrong laser fields: Review and developments,” *Phys. Rev. E* **92**, 023305 (2015).

- [23] V. Anguelov and H. Vankov, “Electromagnetic showers in a strong magnetic field,” *J. Phys. G: Nucl. Part. Phys.* **25**, 1755–1764 (1999).
- [24] Huai-Hang Song, Wei-Min Wang, Jian-Xing Li, Yan-Fei Li, and Yu-Tong Li, “Spin-polarization effects of an ultrarelativistic electron beam in an ultraintense two-color laser pulse,” *Phys. Rev. A* **100**, 033407 (2019).
- [25] Huai-Hang Song, Wei-Min Wang, Yan-Fei Li, Bing-Jun Li, Yu-Tong Li, Zheng-Ming Sheng, Li-Ming Chen, and Jie Zhang, “Spin and polarization effects on the nonlinear Breit-Wheeler pair production in laser-plasma interaction,” (2021), [arXiv:2102.05882](https://arxiv.org/abs/2102.05882) [physics.plasm-ph].
- [26] Huai-Hang Song, Wei-Min Wang, and Yu-Tong Li, “Generation of polarized positron beams via collisions of ultrarelativistic electron beams,” (2021), [arXiv:2103.10417](https://arxiv.org/abs/2103.10417) [physics.acc-ph].
- [27] Yan-Fei Li, Rashid Shaisultanov, Karen Z. Hatsagortsyan, Feng Wan, Christoph H. Keitel, and Jian-Xing Li, “Ultrarelativistic electron-beam polarization in single-shot interaction with an ultraintense laser pulse,” *Phys. Rev. Lett.* **122**, 154801 (2019).
- [28] Yan-Fei Li, Rashid Shaisultanov, Yue-Yue Chen, Feng Wan, Karen Z. Hatsagortsyan, Christoph H. Keitel, and Jian-Xing Li, “Polarized ultrashort brilliant multi-GeV γ rays via single-shot laser-electron interaction,” *Phys. Rev. Lett.* **124**, 014801 (2020).
- [29] Yan-Fei Li, Yue-Yue Chen, Wei-Min Wang, and Hua-Si Hu, “Production of highly polarized positron beams via helicity transfer from polarized electrons in a strong laser field,” *Phys. Rev. Lett.* **125**, 044802 (2020).
- [30] Huai-Hang Song, Wei-Min Wang, Jia-Qi Wang, Yu-Tong Li, and Jie Zhang, “Low-frequency whistler waves excited by relativistic laser pulses,” *Phys. Rev. E* **102**, 053204 (2020).